Performance Measurements of a Theoretical Positron Emission Tomography Scanner Model "T2PET-NSBD" Dedicated to Plant Imaging using Monte Carlo Simulations

Issam Youbi[1*], *Rahal Saaidi*[2,3], Tarek EL Bardouni[4] and *Otman EL Hajjaji*[4]

[1]Institut de Física d'Altes Energies (IFAE), Universitat Autònoma de Barcelona (UAB), Bellaterra, Barcelona, Spain
[2]Mohamed VI Polytechnic University, Benguerir, Morocco
[3]Faculty of Science, Mohammed V University, Rabat, Morocco
[4]Faculty of Science, Abdelmalek Essaadi University, Tetouan, Morocco

Abstract. This work focuses on the performance measurement of a theoretical scanner with an extended Axial FOV for plant Imaging, which is based on the block detector of Naviscan PEM Flex Solo II scanners using the Geant4 Application for Tomographic Emission (GATE) [1,2], we named it T2PET-NSBD (**T**heoretical **P**lant **PET** based on **N**avi**S**can Flex Solo II **B**lock **D**etector) [3,4]. The study aimed to assess the performance of the scanner according to the NEMA NU 4-2008 protocol and compare the results with other experimental data.[5] The findings of this research revealed better performance for this simulated theoretical scanner. Notably, it was observed that minimizing coincidence time windows led to improvements in the NECR (Noise Equivalent Count Rate) and True count rate performance. Additionally, employing non-paralyzable dead time instead of paralyzable dead time resulted in increased NECR. The performance of the T2PET-NSBD scanner was evaluated using various methodologies using different phantoms, including the assessment of spatial resolution, uniformity, recovery coefficients, spill-over ratios, and its application in plant imaging. These evaluations provided valuable insights into the scanner's capabilities and limitations in different imaging scenarios. Overall, this work contributes to the understanding of the performance characteristics of the improvised scanner and highlights the importance of optimizing parameters such as coincidence time windows and dead time for enhanced imaging performance. The results obtained from this study can be valuable for further advancements in PET scanner design and optimization, ultimately benefiting the field of medical imaging.

Keywords: PET scanner, Simulation, Plant imaging, GATE, Tomographic Image Reconstruction, NEMA Protocol, Coincidence Time Window, Dead Time.

* Corresponding author: iyoubi@ifae.es

1 Introduction

Positron Emission Tomography (PET) is a medical imaging technique that uses a radioactive tracer that has special characteristics of the β^+ emitter; a ”carrier” molecule that confers biological specificity is typically involved in the complexation process to visualize the 3D distribution of biological processes in target organs.[6] PET identifies abnormalities by utilizing their metabolic properties rather than their anatomical density.[7] The positrons are detected as two 511 keV photons in opposite directions when they annihilate with electrons in the target organ. Simultaneous detection of these photons allows precise localization of biological processes in target organs.[8] Opposing sensitive detectors, mainly Scintillators, capture the gamma-ray pairs generated from the annihilation of positrons.[9]
The implementation adheres to the manufacturer's specifications by utilizing a Coincidence Time Windows (CTW) and a Dead Time module designed for a specific volume within the Sensitive Detector system. These coincident photons, also known as events, are then recorded and stored in matrices or sinograms. An image reconstruction algorithm processed the sinograms to recover the underlying radioactivity distribution. This process indirectly maps the functional processes that generate the distribution of positron emitters.
Modern PET scanners are combined with computed tomography (CT) systems to provide more precise anatomical information. This fusion of imaging modalities, known as PET/CT, allows for a better correlation between metabolic activity and anatomical structures. It can create complex corrected PET images by multiplying emission scans with attenuation correction maps generated by X-ray CT. [10] This process increases count rates and spatial resolution, improving overall clinical status, diagnosis, development, and treatment planning. In addition, physical effects such as attenuation and diffusion can disrupt the image formation process. [11] Physiological factors, such as patient motion, can also affect image reliability. Additionally, effects associated with tomographic reconstruction techniques can play a role in overall image quality.[12]
For this purpose, Monte Carlo simulations serve as a valuable and effective tool for enhancing image quality in various applications. They enable the study of how components, geometry, and camera acquisition parameters influence the system configuration, allowing for optimization. Several Monte Carlo packages, such as GEANT4, MCNP, and EGSnrc, are widely used to model and evaluate nuclear medicine imaging systems.
The OpenGATE collaboration developed a key simulation tool called the Geant4 Application for Tomographic Emission (GATE).[1,2] GATE has a particular focus on the modeling of tomographic imaging systems such as PET, SPECT, and CT.
Utilizing the Geant4 (Geometry and Tracking) Monte Carlo simulation framework, GATE provides an easy-to-use platform for quickly creating realistic models of tomographs without the need for $C++$ code.[13] GATE includes specific modules necessary to perform realistic simulations, including modules managing time and time-dependent processes (detector and source movements, radioactive decay, and dynamic acquisitions), complex source distributions, and an easy description of scanner geometry. One of the most remarkable features of this package is its capability to synchronize all time-dependent components, enabling a cohesive description of the acquisition process. For this study, our focus lies specifically on simulating PET scanners.
The main purpose of this work is to measure our T2PET-NSBD scanner's performance throughout Monte Carlo simulations. Our PET is an enhanced version of the Naviscan Flex Solo II breast PET scanner. In addition, the impact of various parameters such as coincidence window time, dead time, and block/crystal gap on count rate performance and spatial resolution will be investigated. The ultimate goal is to optimize image quality through these analyses.

 https://doi.org/10.1051/e3sconf/202568000046

2 The National Electrical Manufacturers Association Protocol

The performance measurements with the simulation code involve comparing the results obtained from the simulation under the same conditions as the real experimental acquisition protocol. This comparison is done by comparing the simulated results with the experimental results using a test object with a known activity distribution or published results. To ensure better validation, it is recommended to apply the same treatment and analysis to both the simulated and experimental data. The National Electrical Manufacturers Association (NEMA) performance measurements protocol NU 4-2008 is widely accepted as the standard methodology for assessing the performance of PET systems. This protocol provides detailed instructions for measuring reference figures, including the experimental protocol, data acquisition, and calculation of reference parameters. Manufacturers of clinical PET systems typically calculate the experimental results according to the NEMA standards protocol. The validation of Monte Carlo code for PET scanners involves calculating performance parameters such as spatial resolution, sensitivity, noise equivalent count rate, scatter fraction, and image quality measurement suitable for whole-body imaging, following the NEMA protocol.[5]

3 Creation of the T2PET-NSBD scanner

3.1 The idea

We have planned to use a PEM scanner, which refers to positron emission mammography or positron emission tomography, dedicated to breast imaging, since our objective is to apply it on plants and shape it as a PET scanner instead of two moving detector panels, to allow us comprehensive data acquisition without detector motion, and to operate multi-coincidence mode.

We decided to work with PEM SOLO FLEX-II block detectors [3], especially the one designed and manufactured by NaviScan PET Systems [4], shown in Figure 1 on the left, which is designed to provide high-resolution images of the breast with greater detail compared to conventional breast imaging techniques. It offers tomographic imaging capabilities, allowing for the visualization of lesions with a resolution as low as $1.8\,mm$ which meets the NU 4-2008 criterion.[5,14] This high-resolution imaging enables clinicians to gather valuable clinical data for both invasive and non-invasive breast diseases throughout the continuum of care, from initial staging to post-surgical disease management. **Table 1** shows the characteristics of the scanner.

Table 1. *Characteristic of clinical NaviScan PEM SOLO FLEX-II as two panels. [15]*

Detector Material	LYSO
Crystal Dimensions (mm^3)	2 x 2 x 13
Crystal Array per	13 x 13
Number of crystals per block	169
Total number of crystals	4056
Field of view (mm)	164 x 240

3.2 Geometry of T2PET-NSBD scanner using GATE.

For T2PET-NSBD scanner geometry we thought of extending the detector to fill all the space without the need of moving it ($\pm x$) directions, then we made 6 same detectors to be round shaped and Cylindrical PET so that we don't need to move the detector or the phantom itself, with a little change in the number of blocks (5 instead of 6) the FOV, see **Figure 1** on the right. **Table 2** shows the updated characteristics of our PET scanner.

Table 2. *Characteristic of T2PET-NSBD.*

Detector Material	LYSO
Crystal Dimensions (mm^3)	2 x 2 x 13
Crystal Array per	13 x 13
Number of crystals per block	169
Total number of crystals	60840
Axial Field of view (mm)	326
Diameter Ring (mm)	240

Our objective is to improve the system's coverage of the imaging field and simplify the scanner mechanics. This will result in faster imaging times and/or higher spatial resolution, which can provide significant advantages for specific imaging applications. By optimizing these factors, we aim to enhance the overall image quality.

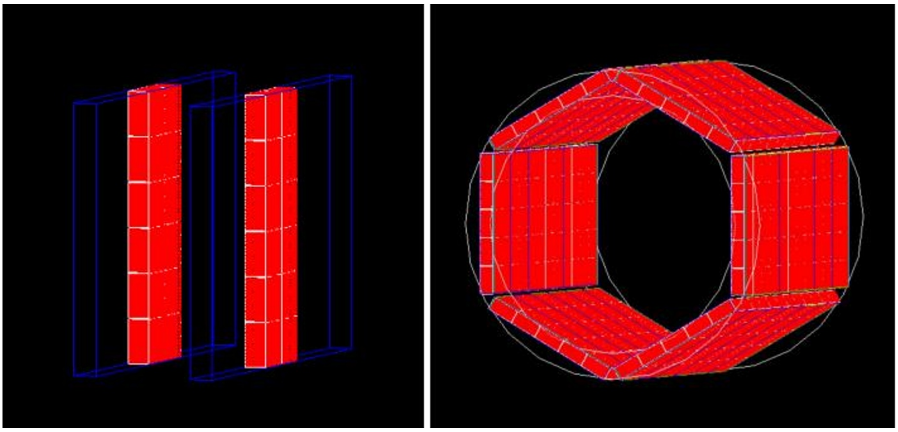

Figure 1. *On the right, T2PET-NSBD geometry, and on the left, the original geometry of PEM Flex Solo II Naviscan, both visualized using GATE QT.*

3.3 Detections of our PET scanner

The generated root file provides various parameters for exploration, including options for generating graphs and figures that depict different positions of the scanner and phantom. ***Figure 2*** illustrates different positions of T2PET-NSBD detection. The axial detection analysis reveals uniformity in the detected signals within each block, demonstrating consistent performance across the scanner's axial plane. On the other hand, the transaxial detection analysis highlights the presence of the scanner ring comprising six detectors, capturing signals from various angles around the imaging region.

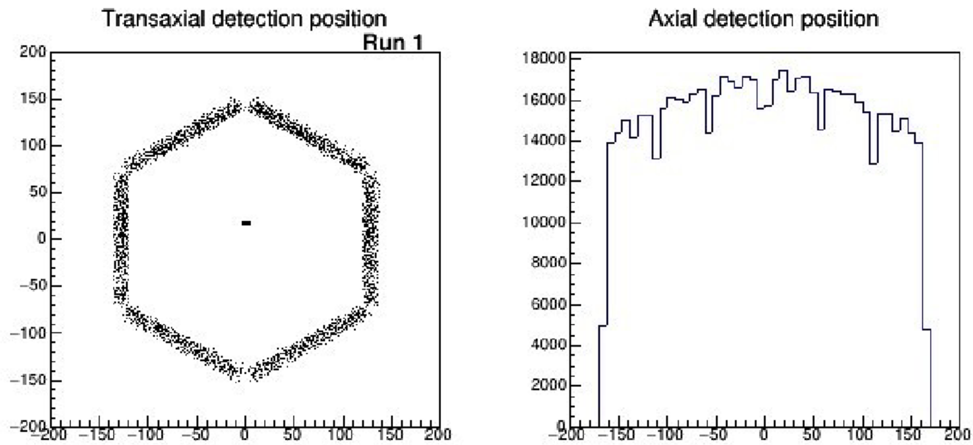

Figure 2. *Axial and transaxial detections over the field of view, generated from the simulation of the* $5MBq$ *linear source.*

4 Performance measurement of the T2PET-NSBD using GATE

To validate the accuracy of our simulation, we have applied loads of simulations of standard performance parameters recommended by the National Electrical Manufacturers Association (NEMA). These parameters include Sensitivity (S), Noise Equivalent Count Rate (NECR), Scatter Fraction (SF), and Image Quality. Additionally, we obtained true count rates from the simulations, further contributing to the comprehensive evaluation of the scanner's performance.[5]

4.1 Scatter Fraction

The objective of this standard is to evaluate the sensitivity of the system to scattered radiation, the impact of system dead time, and the generation of random events at different levels of source activity. The NU 4-2008 Standards specify a testing procedure involving multiple scans of a cylindrical scattering phantom with an inner diameter of $50\ mm$ and height of $150\ mm$. The line source insert was positioned off-center, and the phantom was constructed using high-density polyethylene material with a density of $0.96\ g/cm^3$. A hole with a diameter of $3.2\ mm$ was drilled parallel to the central axis at a radial distance of $17.5\ mm$. The initial activity should be sufficiently high to measure the peak true and peak NECR (Noise Equivalent Count) event rates, while the final activity should be low enough to maintain a random event rate to true event rate ratio of less than 1%.
This protocol ensures an accurate assessment of the system's performance under various activity conditions and provides valuable information on the system's ability to handle scattered radiation and random events. ***Figure 3*** shows the visualization of the NECR and scatter fraction phantom, which is also called rat phantom used to measure the count rates and will be used to calculate the NECR in the following section.[15]

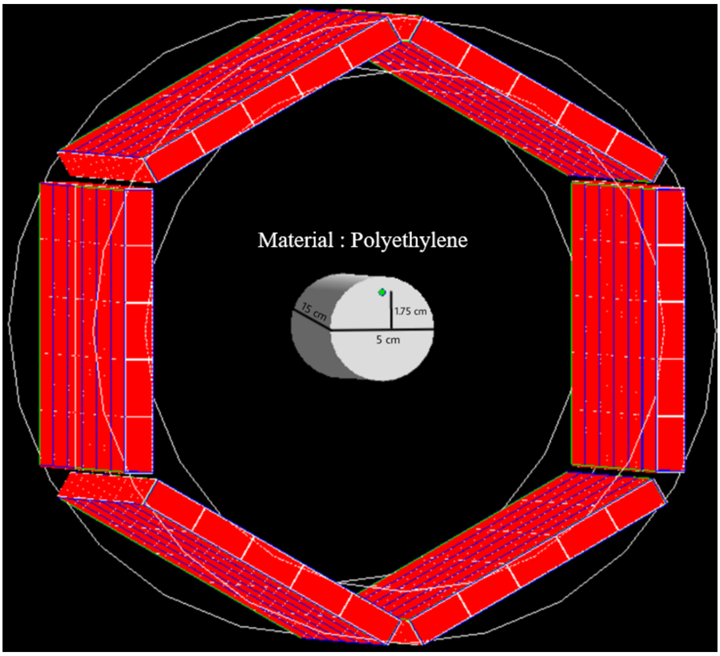

Figure 3. *Visualizing NECR phantom in the T2PET-NSBD scan using GATE QT.*

In the results obtained, for an activity of $0.5\ MBq$, the percentage of random coincidences was found to be less than 1% compared to the true unscattered coincidences. The global scatter fraction was calculated to be 0.189071. These findings indicate that the system's performance at this activity level is characterized by a low occurrence of random coincidences and a relatively moderate level of scatter events.

4.2 Sensitivity

The PET scanner sensitivity is the detection efficiency of a coincidence event when a radionuclide is located in the scanner FOV. We used a point source ($0.3\ mm$ diameter source enclosed in an acrylic cube of $10\ mm^3$) with an activity of $20.4\ kBq$. As the sensitivity is defined by $S = \frac{T}{A}$, where T is the true coincidence count Rate (cps), and A is the source activity, we obtained:

$$S = \frac{3220}{20400} = 0.158\ cps/Bq \qquad (1)$$

4.3 Noise Equivalent Count Rate

A more informative parameter called the Noise Equivalent Count Rate (NECR) has been introduced to assess image quality. The NECR provides valuable information about the primary data quality, specifically regarding the effects of dead time, random rates, and scatter on the scanner's ability to accurately measure the true count rate of events and eliminate random and scatter coincidences during acquisition. Although the NECR does not directly correlate with final image quality, it offers insights into the overall performance of the scanner.[16]

The NECR is typically defined by the following equation:

$$NECR = \frac{T^2}{T+S+R} \qquad (2)$$

In the given context, T represents the count rate of true events, while S represents the count rate of scatter events, and R represents the count rate of random events. Our study yielded promising results that contribute to the current understanding of the phantom, such as the count-rate measures.

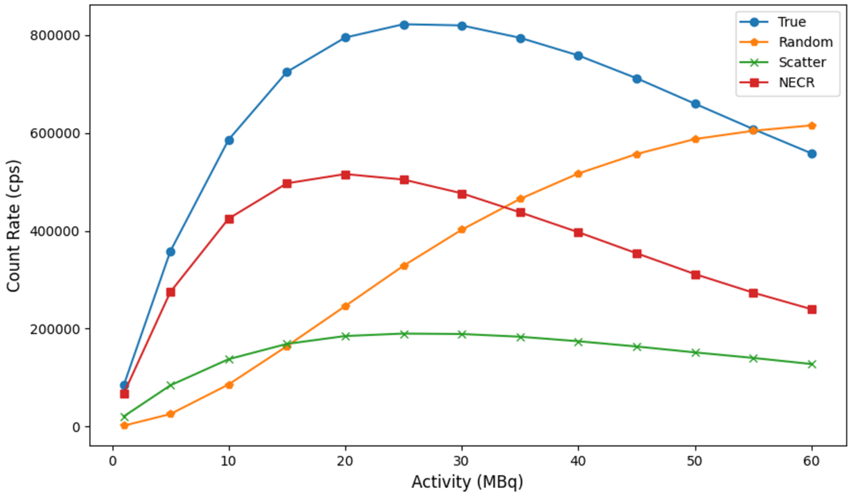

Figure 4. *NECR, True, Random, and Scattered events as a function of the source activity.*

We didn't apply the time of flight (TOF), which is the time it takes for particles or photons to travel from the source to the detector. We applied an ^{18}F line source, with different activities in the same run, these activities are $1, 5\ to\ 60\ MBq$ with a step of 5, the simulation is run in CNRST/HPC-MARWAN [17] with a simple script that goes from the first activity to last one generating root files of each activity. We applied another C script for each root file to convert it to a text file. The generated text file displays various measures, including true unscattered coincidences, random coincidences, scattered coincidences, global scatter fraction, and most importantly, NECR. Later, we took these results and plotted them in a single plot using Python code.
Figure 4 shows the count rate of our parameters mentioned earlier in the function of activity. As you may notice, we got the peak in $25\ MBq$ in true unscattered coincidences, and in $20\ MBq$ in NECR.

4.4 Influence of Coincidence Time Window on Count Rate performance

In small animal PET scans, the coincidence time window is typically shorter than in clinical PET scanners due to the faster decay time of positron-emitting isotopes used in small animal imaging.[18] This narrower time window helps reduce random coincidences. The coincidence time window for small animal PET scanners can range from sub-nanoseconds to a few nanoseconds, with values between 1 and 10 nanoseconds being common.[19]

 https://doi.org/10.1051/e3sconf/202568000046

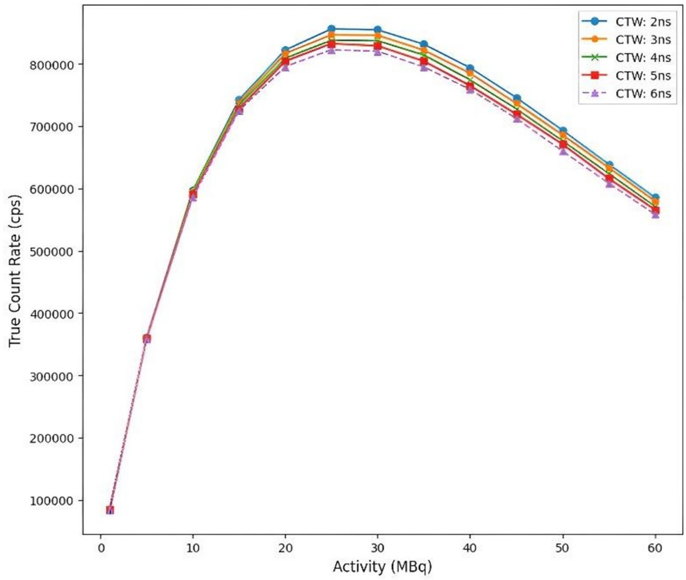

Figure 5. *True unscattered events in different coincidence time windows.*

However, it's important to consult the manufacturer's documentation for the specific coincidence time window set for a particular small animal PET scanner. In this study, the GATE platform was used to assess the impact of altering the coincidence window time on the True Unscattered Coincidences (***Figure 5***) and the Noise Equivalent Count Rate (NECR) (***Figure 6***).

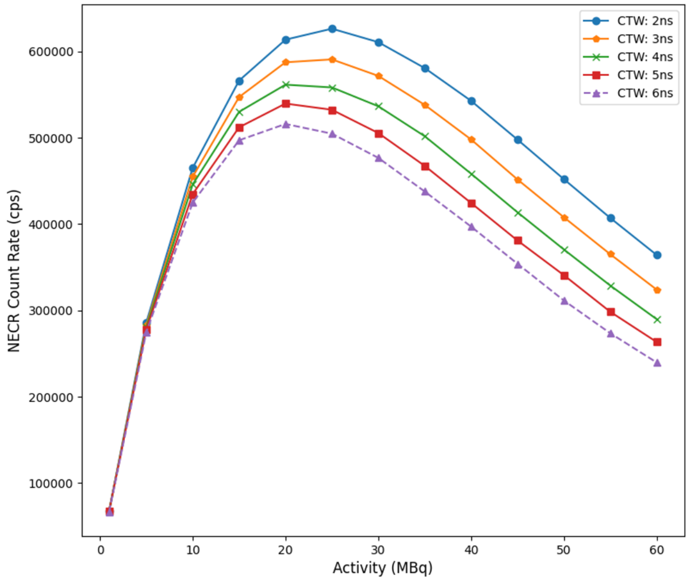

Figure 6. *NECR unscattered events in different coincidence time windows.*

The investigation explored coincidence timing windows from 2 to 6 ns in PET imaging. Results indicated that lower activity concentrations exhibited stable parameters regardless of

window variation, the peak was for the true events in the activity of 25 Mbq for all time windows (6 to 2 ns) showing an increase of events recorded of 4%, and the peak in NECR was in 20 Mbq for all timing windows except for the time windows of 2 and 3 ns showing an increment of 21%. However, higher activity concentrations showed a slight increase in true rates with shorter windows, indicating improved detection of unscattered events.
These findings underscore the importance of considering coincidence window time for PET imaging, particularly at higher activity levels. Setting the lower limit at 2 ns for small animal PET scans in a PEM system optimized performance and sensitivity. This deliberate choice aligns with our system's requirements and ensures accurate imaging within timing constraints. Adhering to this range enables reliable experimentation and consistent results within our specific PEM system configuration.

4.5 Influence of Dead-Time on Count Rate performance

Next in our simulations, we tried to see the influence of the dead time parameter to run it in its two different modes which are paralyzable and non-paralyzable dead time, and note that we didn't change its value which was fixed in 1000 ns in the whole work, ***Figure** 7* shows the results we obtained. We tried to examine the influence of the dead time parameter by running it in two different modes: paralyzable and non-paralyzable dead time. It is worth noting that the value of this parameter remained constant at 1000 ns throughout the study. As observed, the counting rates are high. A notable observation is that the loss of events is more pronounced when paralyzed dead time is present compared to the non-paralyzable dead time scenario, showing an increase of 23% in NECR events. This indicates that the paralyzed dead time effect has a greater impact on event loss under high counting rate conditions. The phenomenon of paralyzed dead time refers to the time interval during which a detector remains unresponsive after detecting an event, leading to a temporary inability to detect subsequent events.[20] The increased event loss in the paralyzed dead time scenario suggests a higher level of inefficiency and reduced accuracy in event detection and measurement at high counting rates.

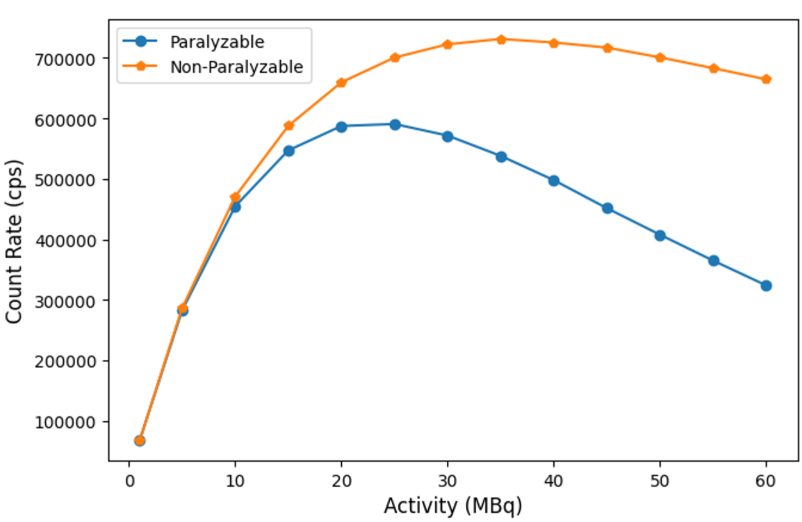

Figure 7. *NECR calculated in paralyzable and non-paralyzable Dead Time.*

4.6 The Mini-Derenzo phantom test over T2PET-NSBD

The Mini-Derenzo or Miniature Derenzo phantom is a cylindrical phantom made of acrylic that is commonly used to evaluate the spatial resolution of small animal positron emission tomography (PET) scanners. It consists of six small rods with varying diameters and spacings, which simulate structures found in small animals.
Our investigation produced encouraging outcomes that enhanced the existing knowledge of the phantom, including the reconstructed images obtained with CASToR.[21] To provide a demonstration of our process, we followed the following steps:

- First step: We initiated the simulation by running a MATLAB script, which generated six PBS (Portable Batch System) scripts for each job. Additionally, a shell script was created to submit all the jobs. These scripts were executed using the shell script on the MARWAN HPC cluster, resulting in the production of six root files.
- Second step: We merged all six root files into a single file for further analysis.
- Third step: We utilized the CASToR image reconstruction technique to generate images of the phantom. This involved executing specific commands in the terminal to obtain the desired output files.
- Final step: We visualized the final image (HDR format) using Fiji ImageJ,[22] allowing for a comprehensive examination of the reconstructed image.

By following this workflow, we successfully simulated the phantom, merged the files, performed image reconstruction, and visualized the reconstructed image using Fiji Im ageJ. The Mini-Derenzo insert of $50\,mm$ diameter and $20\,mm$ height, constructed of PMMA, features fillable hot cylinders with diameters of $5, 4, 3, 2, 1.5,$ and $1\,mm$ in six distinct regions, see ***Figure 8***.

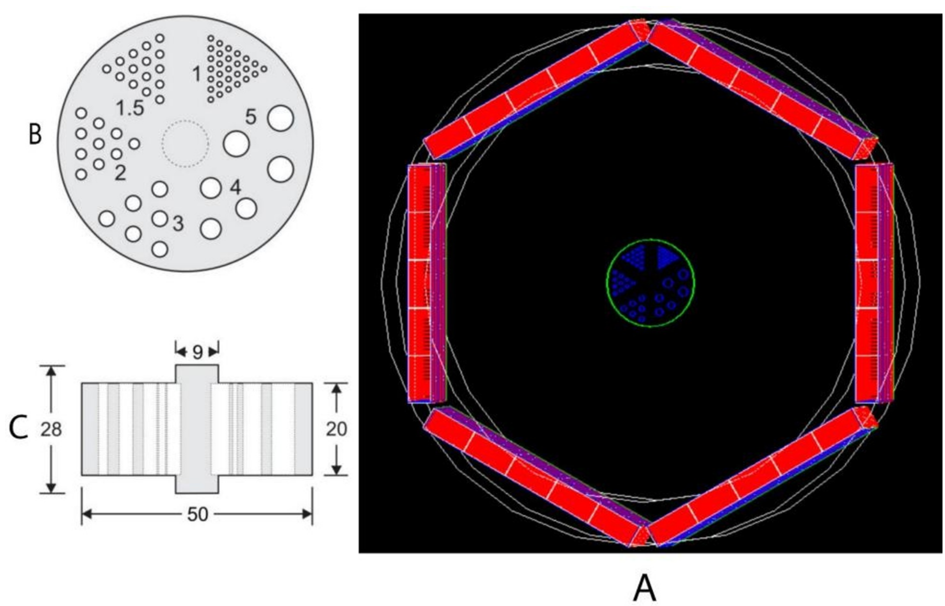

Figure 8. *A: Visualizing the Mini-Derenzo phantom in T2PET-NSBD scan using GATE QT. B, C: The various components of the Mini-Derenzo phantom can be observed from both the top and lateral views. [23]*

The center-to-center distance between these hot spots is twice the diameter of each hot spot. During image reconstruction, random events are corrected by subtracting the events detected in the delayed window. However, scatter and attenuation are not accounted for in the image reconstruction process.

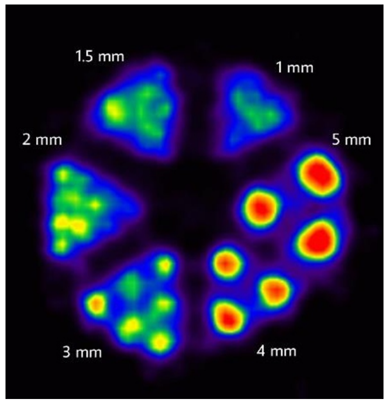

Figure 9. *Mini-Derenzo final image using a filter in CASToR command.*

Figure 9 displays the reconstructed image using CASToR and viewed with FijiImageJ, demonstrating the scanner's ability to resolve the region with a $2\,mm$ diameter. This phantom serves as a valuable tool for assessing the spatial resolution capabilities of small animal PET scanners. We also applied a profile plot to prove the 2 mm region resolving as in ***Figure 10***.

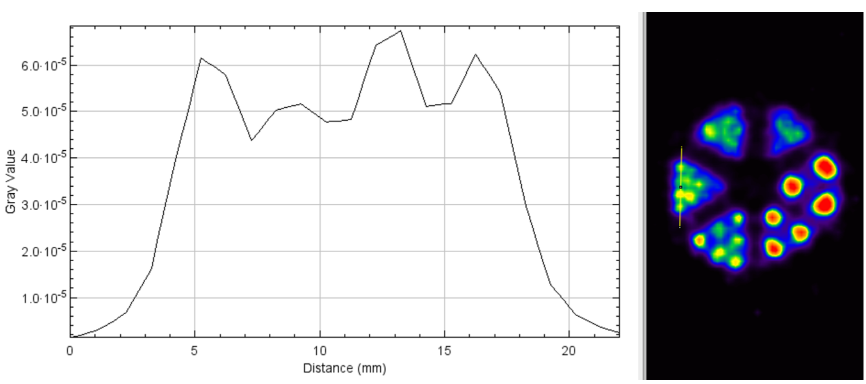

Figure 10. *Profile analysis of 2mm rode.*

The typical approach for evaluating spatial resolution involves determining the mini mum size of the hot rods that can be visually distinguished in the resulting in-plane image. However, this assessment can be challenging due to variations in contrast among the hot rods within a given pie segment. As a result, the interpretation of spatial resolution based solely on hot rod visibility can be ambiguous.

4.7 Image Quality phantom test over T2PET-NSBD

An image quality phantom is a standardized test object used to evaluate the imaging performance of PET scans. It simulates real-life clinical scenarios and includes different tissue types, contrast levels, and spatial resolutions. By using an image quality phantom, researchers and medical professionals can assess the capabilities and limitations of a PET scanner in a controlled manner.

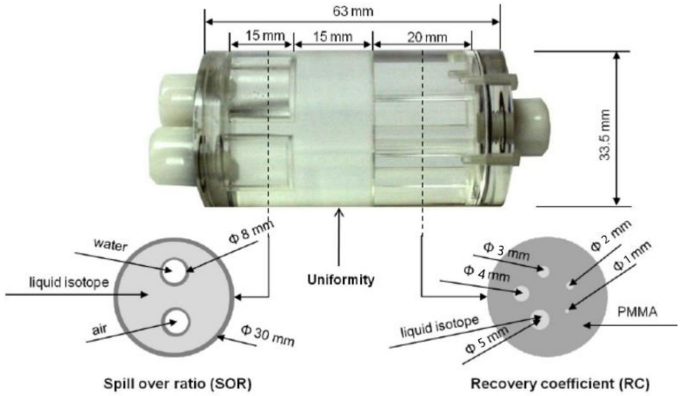

Figure 11. *A schematic of NEMA NU4-2008 image quality phantom.[5]*

It allows for testing and comparing image quality across scanners or imaging protocols, including factors such as spatial resolution, contrast sensitivity, noise levels, and overall image fidelity. Image-quality phantoms typically incorporate inserts or components that mimic specific anatomical structures or features, with different materials and physical properties. They may also include contrast agents or signal modifiers to replicate contrast variations seen in clinical settings.

To evaluate the impact of various reconstruction algorithms and filters on image quality for ^{18}F, a NEMA NU4 phantom (***Figure 11***) was employed. PET data for ^{18}F with an activity of 0.18 MBq were acquired using an energy window of $350 \sim 750\ keV$. The datasets were not subjected to normalization, attenuation, or scatter corrections. The same reconstruction protocols employed for measuring the spatial resolution in the Mini-Derenzo phantom were used. The image matrix size was $60 \times 200 \times 300\ mm^3$. The image quality assessment included evaluating Uniformity, Recovery coefficients, and spillover ratio. ***Figure 12*** shows the phantom simulated with GATE.

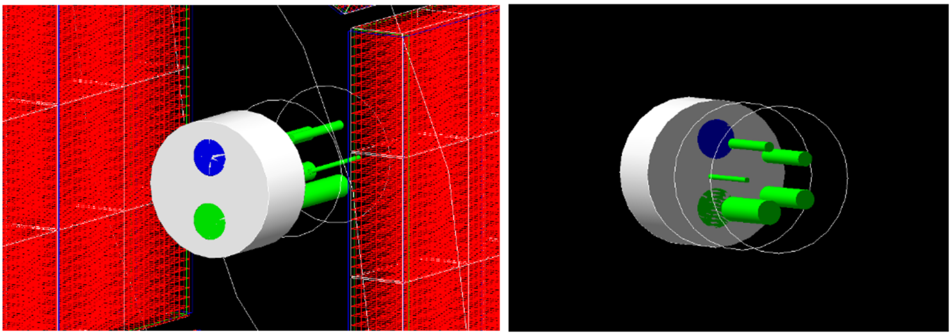

Figure 12. *I-Q phantom visualized with Gate QT.*

In this study, the three cylindrical containers along with their inserts were simultaneously positioned within the field of view (FOV), adhering to the specified activities and data acquisition parameters. Subsequently, the evaluation of uniformity, recovery coefficients (RCs), and spillover ratios (SORs) followed the guidelines outlined in the NEMA NU 4-2008 protocol. For all evaluations, volumes of interest (VOIs) with a length of $10\ mm$ along the z-axis were employed. These VOIs corresponded to the central in-plane images of the phantom, specifically 11 slices.

4.7.1 Uniformity

To assess uniformity, a cylindrical container was filled with a radioactive solution consisting of ^{18}F mixed with water. Within the uniform region of the IQ phantom, a cylindrical volume of interest (VOI) with a diameter of $22.5\ mm$ (75% of the internal diameter) and a length of $10\ mm$ was selected. From this VOI, the mean, maximum, and minimum pixel values ($I_{U,mean}$, $I_{U,max}$, $I_{U,min}$), as well as the standard deviation (STDU), were extracted to further quantify uniformity. The calculation of the percentage standard deviation followed the guidelines specified in the NEMA NU 4-2008 protocol as follows:

$$\%STD_U = (SSTD_U / I_{U,mean}) \times 100$$

Figure 13 represents the reconstructed uniformity image obtained using the CASToR. The image provides insights into the distribution and consistency of the measured values across the entire field of view. ***Table 3*** presents detailed numerical results derived from the measurements performed on the 11 slices.

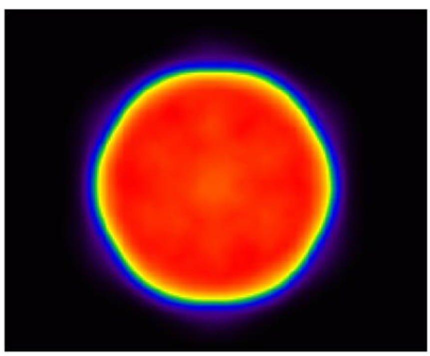

Figure 13. *Uniformity image reconstructed with CASToR.*

Table 3. *Uniformity values with T2PET-NSBD.*

Radionuclide	$I_{U,mean}$	$I_{U,min}/I_{U,max}$	STD_U	$\%STD_U$
^{18}F	62577.8 ± 586.38	0.84	2172.665 ± 266.929	3.47 ± 0.43

4.7.2 Recovery Coefficients

As in ***Figure 11***, the 5 radioactive source fillable rods ($1, 2, 3, 4$, and $5\ mm$ in diameter) at the bottom of the cylinder (length: $20\ mm$ and diameter: $30\ mm$) were used to determine the RCs. To determine the RCs, a circular ROI of twice the rod diameter was drawn around each rod. The positions of the maximum values in the ROI were used to plot the line profile through the rods. RCs were defined as the ratio between the measured maximal values on the

profile through the rods and the mean value in the uniform area. 11 image slices were averaged to produce a single slice.
Circular ROIs were selected around each rod with twice their diameter and, from these, I_{max} was measured. Recovery coefficients were calculated for each rod size as the ratio of I_{max} and $I_{U,mean}$ obtained in the previous section.
Figure 14 shows the recovery coefficients image reconstructed using CASToR, and **Table 4** shows the results obtained with the measurements of the 11 slices.

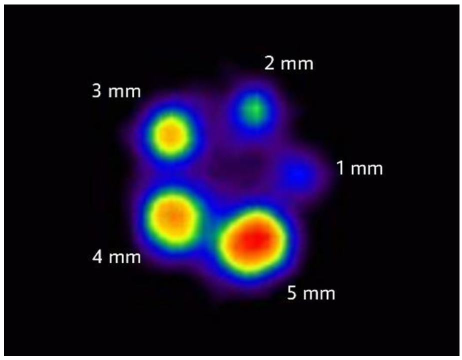

Figure 14. *Recovery Coefficients image reconstructed with CASToR.*

Circular ROIs were selected around each rod with twice their diameter and, from these, Imax was measured. Recovery coefficients were calculated for each rod size as the ratio of Imax and $I_{U,mean}$ obtained in the previous section.
Figure 14 shows the recovery coefficients image reconstructed using CASToR, and ***Table 4*** shows the results obtained with the measurements of the 11 slices.

Table 4. *Recovery coefficients of the PEM system as a function of the hot rod diameter.*

Rod $\varnothing$ $(\boldsymbol{mm})$	$^{18}\boldsymbol{F}$	
	$\boldsymbol{RC}$	$\%\boldsymbol{STD_U}$
1	0.43	3.55
2	0.93	13.45
3	1.03	13.89
4	1.02	9.28
5	1.4	12.9

Table 4 presents the recovery coefficients (RCs) for the ^{18}F radionuclide, corresponding to different rod diameters. The results indicate that as the cylinder diameter increases, the RCs also increase. This observation aligns with expectations, as a larger diameter reduces the impact of the partial volume effect. Notably, complete contrast recovery was achieved with ^{18}F and the largest rod diameter of 5 mm. However, there was an anomaly in the RC values for the 4 mm diameter cylinder, which can be attributed to several factors. Possible measurement errors in CASToR may have affected the accuracy of the data. Additionally, the positron energy is known to have a significant influence on performance, with improved results observed.

4.7.3 Spill-over ratios

The upper section of the uniform region contained two empty spaces, each with a length of 15 mm, an inner diameter of 8 mm, and an outer diameter of 10 mm. One space was filled with air, while the other was filled with non-radioactive water. The spill-over ratio (SOR) was calculated by dividing the mean value within each cold cylinder by the mean value in the uniform area $I_{U,mean}$. Even though both cylinders are non-radioactive, the presence of scattered coincidences and random coincidences can contribute to activity in the non-radioactive cylinder. By calculating the SOR values in these nonradioactive regions, we can determine the impact of scattered or random coincidences.

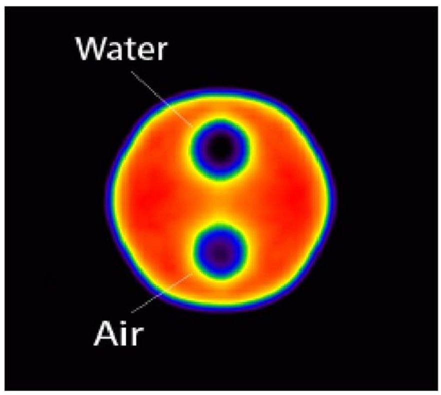

Figure 15. *Spill-over ratios image reconstructed with CASToR.*

To calculate the SOR, cylindrical volumes of interest (VOIs) with a length of 7.5 mm and a diameter of 4 mm were drawn within the compartments filled with air and water. ***Figure 15*** shows the spill-over ratios image reconstructed using CASToR, and ***Table 5*** shows the results obtained with the measurements of the 11 slices.

Table 5. *The spill-over ratios (SOR) for air and water using ^{18}F were calculated based on the mean intensity values of uniformity as shown in Table 3.*

Material	^{18}F	
	SOR	$\%STD_U$
Water	0.15	9.87
Air	0.27	9.37

4.7.4 Discussion

Our findings indicate a uniformity variation of 3.47% for ^{18}F, which is consistent with the results reported by Luo et al.[15] in the standard resolution mode. It is noteworthy that our study utilized an IQ phantom with different dimensions and different positioning within the scanner.
The degradation of signal recovery caused by limited spatial resolution in the imaging system is a well-established phenomenon. This leads to lower signal intensities for small objects compared to their true activity, primarily due to partial volume effects. The recovery

coefficients obtained in our study, which range theoretically from 0 to 1, demonstrate the expected trend. As the diameter of the hot rod increases, the recovery coefficients monotonically increase, eventually reaching a value of unity for the largest hot rod ($5\ mm$ in diameter) for ^{18}F.
Luo et al.[15] reported maximum recovery coefficients (RCs) of up to 0.5 for the $5\ mm$ hot rod diameter for this radionuclide. In contrast, our analysis yielded RCs of 1.4 for the same rod diameter. This discrepancy can be attributed to the difference in phantom orientation during their experimental setup. When comparing our results, it becomes evident that high-energy positrons have a detrimental effect on the RC values, which can be attributed to the significant impact of the positron range.
The spill-over ratios (SORs) for the ^{18}F radionuclide and both non-radioactive materials demonstrate large values, averaging at 23%. These values arise from various factors such as scattered photons, non-zero positron range, random coincidences, and other effects that are not accounted for during image reconstruction. It is not surprising that higher SOR values have been reported in small-animal PET scanners that lack attenuation and scatter corrections, as observed in studies by Ko et al.[24] and Omidvari et al.[25], aligning with our findings. To ensure the significance of this test, it is imperative to implement appropriate corrections for physics effects.
Our study emphasizes the impact of positron range, spatial resolution degradation, and reduced activity recovery on image quality. Understanding the specific properties of the positron emitter is crucial for accurate interpretation. However, in our theoretical PEM Flex Solo II system, image quality is limited by the reconstruction method and inflexible user interface. The fixed acquisition protocol constrains spatial resolutions in all dimensions. Accounting for neighboring slice information in reconstruction poses challenges for activity quantification. Advanced reconstruction methods incorporating attenuation and scatter corrections are expected to improve image quality.

4.8 Multi-Leaf phantom test

4.8.1 Process and Results

To fulfill our objective of developing an effective scanner for plant imaging, we con ducted tests using a custom-designed multi-leaf phantom, see ***Figure 16***.

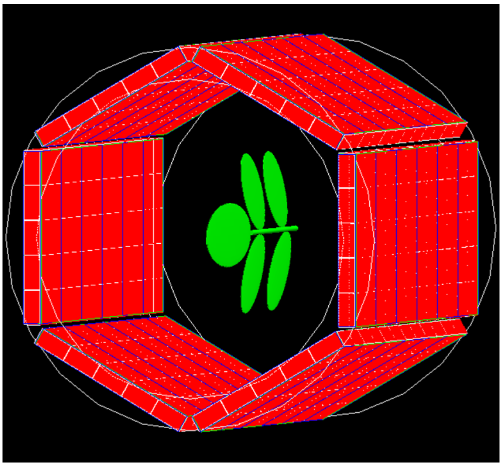

Figure 16. *Visualizing the Multi-Leaf phantom in T2PET-NSBD scan using GATE QT.*

This phantom consists of a cylindrical branch with a height of 120 mm and a radius of 2 mm, resulting in a total volume of 1.508 cm^3. Surrounding the branch, there are five ellipsoid-shaped leaves. The largest leaf, positioned at the top, has dimensions of 0.5 mm in the x-direction, 20 mm in the y-direction, and 60 mm in the z-direction, contributing a total volume of 3.14 cm^3. The remaining leaves have identical dimensions of 0.5 mm, 20 mm, and 40 mm in the x, y, and z directions, respectively, and are rotated by ±42 degrees. Each of these leaves has a volume of 1.68 cm^3.[26] To ensure consistency across all elements of the phantom, we set an activity of 26.5 kBq for each volume unit. Consequently, the branch exhibits an activity concentration of 39.962 kBq, the top leaf has an activity of 83.21 kBq, and the remaining leaves possess an activity of 44.52 kBq each.

Figure 16 shows the phantom created inside our scanner. To assess the performance of our PET scan, we utilized different radio-tracers for each component of our phantom. Starting from the branch and extending to the final leaf, we assigned distinct isotopes to observe their behavior within the imaging system. The chosen isotopes for each part of the phantom were as follows:

- The branch and the first leaf were labeled with Fluor18 (^{18}F).
- The 2nd to the 5th leaf were tagged with Oxygen15 (^{15}O), Carbon11 (^{11}C), Nitrogen13 (^{13}N) and Phosphorus30 (^{30}P), respectively.

Figure 17 (right) shows the final reconstructed image with CASToR using the root files resulting from running different simulations with GATE. By employing different radiotracers throughout the phantom, we aimed to evaluate the scanner's capability to detect and visualize the distribution of these isotopes within the plant structure.

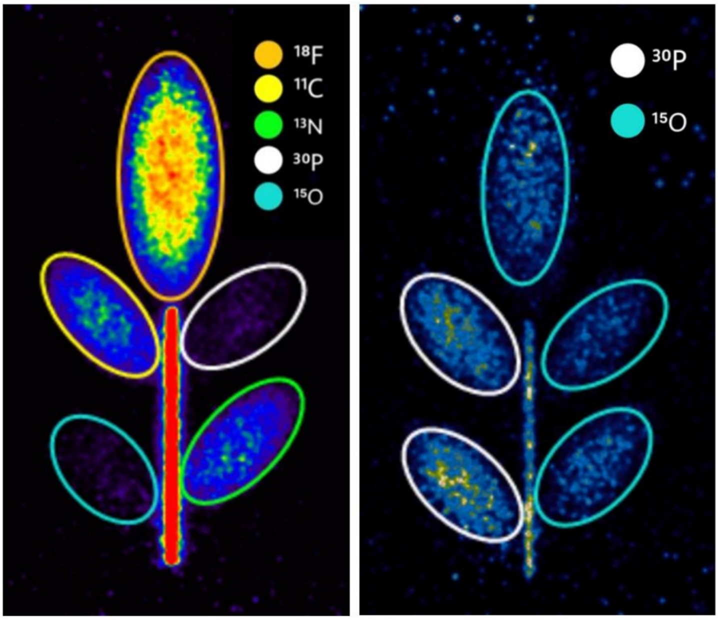

Figure 17. *The final images reconstructed with CASToR showing the distribution of only* ^{30}P *and* ^{15}O *(left) and the distribution of all the radiotracers (right).*

4.8.2 Discussion

This approach allowed us to comprehensively analyze the performance of our PET scan across various radio-tracers and different components of the phantom. It is obvious that the leaves labeled with ^{30}P and ^{15}Oin the simulated scenario (***Figure 17 (left)***) do not exhibit a proper distribution of photons, which can be attached to the positron range and the relatively short half-lives of these isotopes. 30P has a half-life of $2.498min$, while ^{15}O has a half-life of $123s$. The short half-life of these isotopes implies that their radioactive decay occurs rapidly, leading to a decreased number of emitted photons during the imaging process. This reduced photon emission is the cause of the observed lack of distribution in the reconstructed images.
To validate this perspective, we specifically used ^{30}P and ^{15}O isotopes for the different elements of the phantom. The resulting reconstructed image is shown in ***Figure 17 (left)***. The difference in half-life between these isotopes plays a crucial role in image processing. In particular, due to its shorter half-life, ^{15}O does not exhibit significant photon distribution and significantly impacts the quality of the image.
Overall, our study provides valuable insights into the performance and limitations of our PET scanner for plant imaging. Further advancements, such as incorporating correction factors for attenuation and scatter, and using more sophisticated reconstruction methods, are recommended to improve image quality and enhance the accuracy of activity quantification in plant imaging studies.

5 Conclusion

This work has presented a comprehensive exploration of a theoretical PET scanner we developed called T2PET-NSBD which stands for Theoretical Plant PET based on Naviscan PEM Flex Solo II Block Detector. We have delved into the underlying physics, design principles, and practical application of our improvised PET scanner. Throughout the chapters, we have gained a deeper understanding of the intricacies of PET technology, including radiation-matter interactions, system components, image reconstruction algorithms, and performance evaluation. By applying this knowledge to our theoretical PET scanner, we have demonstrated its potential and performance through various experiments and analyses.
It is important to note that the image reconstructions and evaluations presented in this work were performed on our improvised theoretical PET scanner without the use of normalization or correction techniques. This limitation highlights the need for further enhancements and refinements to optimize the scanner's performance in future iterations.
Our objective in the future is to continue improving our PET scanner, drawing in spiration from the Naviscan PEM Flex Solo II system and other established PET technologies. By incorporating advanced normalization and correction methods, we aim to enhance image quality, accuracy, and overall performance. This will enable our scanner to be used by manufacturers and researchers, contributing to advancements in the field of nuclear medicine.

References

[1] Agostinelli S, Allison J, Amako K al, Apostolakis J, Araujo H, Arce P, et al. Geant4—a simulation toolkit. Barrand, et al. Nucl Instruments Methods Phys Res Sect A Accel Spectrometers, Detect Assoc Equip 2003;506(3):250–303.
[2] Strulab D, Santin G, Lazaro D, Breton V, Ch Morel. Gate (geant4 application for tomographic emission): a pet/spect general-purpose simulation platform. Nucl Phys B-

Proceedings Suppl 2003;125:75–79.
[3] MacDonald L, Edwards J, Lewellen T, Haseley D, Rogers J, Kinahan P. Clinical imaging characteristics of the positron emission mammography camera: Pem flex solo ii. J Nucl Med 2009;50:1666–75.
[4] CMR Naviscan Corporation n.d. https://cmr-naviscan.com/.
[5] Association NEM. Performance measurements of small animal positron emission tomographs NU4-2008. NEMA Stand Publ 2008:1–23.
[6] Budinger TF, Vanbrocklin HF, Generator-Produced P, Radiopharmaceuticals R, Radionuclides. P. Positron-Emission Tomography (PET). The biomedical engineering handbook. 2003.
[7] Michael E Phelps. Pet: a biological imaging technique. Neurochem Res 1991;16:929–40.
[8] Massoud TF, Sanjiv S Gambhir. Molecular imaging in living subjects: seeing fundamental biological processes in a new light. Genes Dev 2003;17:545–80.
[9] Lecoq P. Scintillation detectors for charged particles and photons. Part Phys Ref Libr Vol 2 Detect Part Radiat 2020;2:45–89.
[10] Kinahan PE, Hasegawa BH, Beyer T. X-ray-based attenuation cor rection for positron emission tomography/computed tomography scanners. Semin Nucl Med 2003;33:166–79.
[11] Saaidi R, Villafuerte-Villafuerte MR, Sánchez Héctor A, Martínez-Dávalos A. Crystal scatter effects in a large-area dual-panel positron emission mammography system. PLoS One 2024;19.
[12] Havsteen I, Ohlhues A, Madsen KH, Nybing JD, Christensen H, Christensen A. Are movement artifacts in magnetic resonance imaging a real problem?—a narrative review. Front Neurol 2017;8:232.
[13] Saaidi R, Yassine Toufique, Abdelkrim Zeghari, Moursli RC El. Gate simulation study of the siemens biograph mct 20 excel pet/ct system. Polish J Med Phys Eng 2019;25:7–14.
[14] Moliner L, A. J. González, Soriano A, F. Sánchez, C. Correcher, A. Orero, et al. Design and evaluation of the mammi dedicated breast pet. Med Phys 2012;39:5393–404.
[15] Luo W, Anashkin E, Matthews CG. Performance evaluation of a pem scanner using the nema nu 4—2008 small animal pet standards. IEEE Trans Nucl Sci 2010;57:94–103.
[16] Reynés-Llompart G, Sabaté-Llobera A, Llinares-tello E, Martí-Climent JM, Cristina Gámez-Cenzano. Image quality evaluation in a modern pet system: impact of new reconstructions methods and a radiomics approach. Sci Rep 2019;9:10640.
[17] HPC-MARWAN n.d. https://hpc.marwan.ma/.
[18] Saaidi R, Zeghari A, Moursli RC El. Monte carlo simulation of two siemens biograph pet/ct system using gate: Image quality performance. Radiat Phys Chem 2024;218:111653.
[19] Juan José Vaquero, Kinahan P. Positron emission tomography: current challenges and opportunities for technological advances in clinical and preclinical imaging systems. Annu Rev Biomed Eng 2015;17:385–414.
[20] Usman S, Patil A. Radiation detector deadtime and pile up: A review of the status of science. Nucl Eng Technol 2018;50:1006–16.
[21] Thibaut Merlin, Stute S, Benoit D, Bert J, Thomas Carlier, Comtat C, et al. Castor: a generic data organization and processing code framework for multi-modal and multi-dimensional tomographic reconstruction. Phys Med Biol 2018;63:185005.
[22] Schindelin J, Arganda-Carreras I, Frise E, Kaynig V, Longair M, Pietzsch T, et al. Fiji: an open-source platform for biological-image analysis. Nat Methods 2012;9:676–82.
[23] Torres-Urzúa LF, Alva-Sánchez H, Martínez-Dávalos A, García-Pérez FO, Peruyero-Rivas RM, Mercedes Rodríguez-Villafuerte. A dedicated phantom design for positron emission mammography performance evaluation. Phys Med Biol 2020;65:245003.
[24] Ko GB, Kim KY, Yoon HS, Lee MS, Son J-W, Im H-J, et al. Evaluation of a silicon photomultiplier pet insert for simultaneous pet and mr imaging. Med Phys 2016;43:72–83.
[25] Omidvari N, Cabello J, Topping G, Schneider FR, Paul S, Schwaiger M, et al. PET performance evaluation of MADPET4: a small animal PET insert for a 7 T MRI scanner. Phys Med Biol 2017;62:8671.
[26] Saaidi R, Tayalati Y, Fatimy A El. Optimizing positron emission tomography for accurate plant imaging using monte carlo simulations to correct positron range effects. Sci Rep 2025;15:13847.